 CMES, vol.85, no.4, pp.299-328, 2012

Design of Compliant Mechanisms Using Meshless Level Set Methods

Zhen Luo[1], **Nong Zhang**[1], **Tao Wu**[2,3]

Abstract: This paper presents a meshless Galerkin level-set method (MGLSM) for shape and topology optimization of compliant mechanisms of geometrically nonlinear structures. The design boundary of the mechanism is implicitly described as the zero level set of a Lipschitz continuous level set function of higher dimension. The moving least square (MLS) approximation is used to construct the meshless shape functions with the global Galerkin weak-form in terms of a set of arbitrarily distributed nodes. The MLS shape function is first employed to parameterize the level set function via the surface fitting rather than interpolation, and then used to implement the meshless approximations of the discrete state equations. Since the MLS shape function lacks of Kronecker delta function property, a constrained Galerkin global weak-form using the penalty method is applied to enforce the essential boundary conditions. In this way, the shape and topology optimization of the design boundary is just a question of advancing the discrete level set function in time by updating the unknown parameters for the parameterized size optimization. Compared to most conventional level set methods, the proposed MGLSM is able to (1) propagate the discrete level set function and solve the state equations at the same time with one unified set of meshes, (2) avoid numerical difficulties in solving the complicate Hamilton-Jacobi partial differential equations (PDEs), and (3) describe the implicit moving boundaries without remeshing for discontinuities. A benchmark numerical example is used to demonstrate the effectiveness of the proposed method.

Keywords: Complaint mechanisms; Topology optimization; Level set methods; Moving least square (MLS) shape functions; Meshless Galerkin weak-forms.

[1] School of Electrical, Mechanical and Mechatronic Systems, The University of Technology, Sydney, NSW 2007, Australia

[2] School of Software Engineering, Huazhong University of Science and Technology, Wuhan, Hubei 430074, China

[3] Corresponding Author, Tel.: +86 27 8779 3070; Fax: +86 27 8779 2251. E-mail address: wutao1972@mail.hust.edu.cn (Prof. Tao Wu)

1 Introduction

Compliant mechanisms [Howell (2001)] are a relatively new family of hinge-free devices to perform mechanical tasks of transferring and transforming energy, force and motion between different ports. Compared to conventional rigid-link mechanisms, a compliant mechanism can achieve at least a portion of its flexibility via the elastic deformation of one more structural segments triggered by the strain energy. Compliant mechanisms are becoming increasingly popular in a variety of engineering areas over the past [Ananthasuresh and Howell (2005)], due to its great potential in reducing friction, lubrication, assemblage, noise and vibration. Amongst a number of design methods, topology optimization has provided an alternative technique for the systematic design of compliant mechanisms [Sigmund (1997); Howell (2011); Lin, Luo and Tong (2010)].

Topology optimization has recently experienced considerable development with a range of successful applications [Bendsøe and Sigmund (2003)], including the lightweight design of aerospace structures [Luo, Yang and Chen (2006)], and compliant multiphysics actuators [Luo, Tong and Kang (2009); Luo, Zhang, Ji and Wu (2012)]. Essentially, topology optimization consists of a numerical procedure to iteratively redistribute a prescribed amount of material in the design domain subjecting to supports and loads, to determine the best material layout to optimize the design objective under specific constraints. During the past years, several typical topology optimization methods have been developed, including the homogenization method [Bendsøe and Kikuchi (1988)], the SIMP approach [Zhou and Rozvany (1991); Bendsøe and Sigmund (1998)], and the level set-based method [Sethian and Wiegman (2000); Wang, Wang and Guo (2003); Allaire, Jouve and Toader (2004)]. In particular, SIMP has experienced popularity due to its conceptual simplicity and implementation easiness, and a couple of variant SIMP models have also been developed [e.g. Kang and Wang (2011); Wang, Luo and Zhang (2012)].

Recently, the level set method has emerged as an alternative approach to structural shape and topology optimization. The level set method is originally intended for tracking, modeling, and simulating the motion of an interface to achieve complex shape fidelity and topology changes in many fields [Osher and Sethia (1988); Sethian (1999); Osher and Fedkiw (2002)]. Since the landmark work of [Sethian and Wiegmann (2000)], many different level set methods have been developed for shape and topology optimization problems. These methods can be roughly classified into two different categories. The first of which is to evolve the design boundary according to the solutions of the Hamilton-Jacobi PDEs using explicit time schemes [Sethian and Wiegmann (2000); Wang, Wang and Guo (2003); Allaire, Jouve and Toader (2004); Yamada, Izui, Nishiwaki and takezawa (2010)]. How-

ever, it is well known that several unfavorable numerical features are involved in applying the standard level set method to shape and topology optimization of continuum structures. To overcome these numerical difficulties, some alternative level set methods have been developed without directly solving the Hamilton-Jacobi PDEs [e.g. Luo, Tong and Kang (2009); Lin, Luo and Tong (2010); Luo, Zhang, Ji and Wu (2012)]. But it can be found that most of the above level set methods comprise two distinct numerical stages based on two different sets of structured meshes, namely, the propagation of the discrete level set function based on a set of Eulerian grid and the state equations discretization based on a set of Lagrangian mesh. To unify the two different stages will simplify the numerical process in applying the level set method to shape and topology optimization. Since the level set equation is hyperbolic PDEs, it is difficult to unify the two different stages using standard finite element methods due to numerical instabilities.

Over the past, at least 10 different meshfree methods have been developed with a large number of publications [Belytscko, Krongauz, Organ, Fleming, and Krysl (1996); Atluri and Shen (2002); Liu and Gu (2005)]. Amongst these methods, the methods based on Galerkin weak-forms are experiencing popularity, which typically include the element free Galerkin (EFG) method [Belytscko, Lu, and Gu (1994)] and the meshless local Petrov-Galerkin (MLPG) method [Atluri and Zhu (1998)]. In particular, the EFG method [Belytscko, Lu, and Gu (1994)] has been successfully applied to many mechanics problems, because the EFG method in general exhibits good numerical stability and accuracy for solid mechanics problems [Dolbow and Belytscko (1998)]. In EFG methods, the MLS approximation [Lancaster and Salkauskas (1981)] is usually employed to construct the shape function, the Galerkin global weak-form is used to discretize the state equation, and background cells, independent of the field nodes, is included to implement numerical integrations for system matrices. The MLS Galerkin approximation is required to be constrained to enforce the satisfaction of the Kronecker delta function property for the imposition of essential boundary conditions. So in this way the MLS approximation is both consistent and compatible, and one particular attractive property of MLS approximation is that its continuity can be inherited from the continuity of weight functions.

From the literature, it can be seen that there have been a few researches attempted to apply meshless methods to topology optimization of structures [Li and Atluri (2008); Zheng, Long and Xiong and Li (2008); Du, Luo, Tian and Chen (2009); Luo, Zhang, Ji and Wu (2012)]. However, the EFG method with MLS approximation hasn't been applied to level-set models for advanced topology optimization problems of structures, although it is a natural way to combine EFG meshless methods with level-set models. So this study aims to propose a meshless level-set

method for shape and topology optimization of the compliant mechanisms in terms of a set of arbitrarily scattered nodes. The MLS shape function is not only used to parameterize the level set function, but also applied to construct the shape functions for meshless function approximations. The MLS meshless approximation enforced by the penalty method can satisfy the basic requirements for a good meshless approximation. As a result, compared to most conventional level set methods associated with finite element methods, the proposed meshless level set method can be used to unify the two different numerical stages, to avoid numerical difficulties and to handle the moving boundary discontinuities without remeshing.

2 Approximations using MLS shape functions

With the well-known moving least squares (MLS) interpolants in curve and surface fitting [Lancaster and Salkauskas (1981)], the MLS approximation for a general function $u(x)$ at x is defined by

$$u^h(x) = \sum_{J=1}^{m} p_J(x) a_J(x) = \mathbf{p}^{\mathbf{T}}(\mathbf{x})\mathbf{a}(\mathbf{x}) \tag{1}$$

where $p^{\mathrm{T}}(x)$ is a complete polynomial of order m acting as the basis at x. For a linear basis in two dimensional cases, we have the following definition considering $\mathbf{x} = [x, y]$ and $\mathbf{x}_I = [x_I, y_I]$

$$\mathbf{p}^{\mathbf{T}}(\mathbf{x}) = [1, x, y] \tag{2}$$

and $\mathbf{a}(\mathbf{x})$ is the vector consisting of unknown coefficients, which is given as

$$\mathbf{a}^{\mathbf{T}}(\mathbf{x}) = [a_0(\mathbf{x}), a_1(\mathbf{x}), a_2(\mathbf{x}), ..., a_m(\mathbf{x})] \tag{3}$$

where $a_j(x)$ are the parameters related to any given point, which can be determined by minimizing a weighted discrete $\mathbf{L}_2$ norm over all nodes $I \in \{1, 2, ..., n\}$ where the parameters u_I are pre-known.

$$J = \sum_{I=1}^{n} \tilde{w}(\mathbf{x} - \mathbf{x}_I) \left(\sum_{J=1}^{m} p_J(\mathbf{x}_I) a_J(\mathbf{x}) - u_I \right)^2 \tag{4}$$

where n is the number of nodes within the local support of $\mathbf{x}$ where $\tilde{w}(\mathbf{x} - \mathbf{x}_I) \neq 0$. u_I is the nodal parameter of u at $x = x_I$. The minimization of J with respect to the coefficients $\mathbf{a}(\mathbf{x})$ results in a set of linear equations as

$$\mathbf{A}(\mathbf{x})\mathbf{a}(\mathbf{x}) = \mathbf{B}(\mathbf{x})\mathbf{u} \tag{5}$$

Here $\mathbf{u}$ is the vector consisting of the nodal parameters for all nodes inside the support domain, and $\mathbf{u}^{\mathrm{T}} = [u_1, u_2, ..., u_n]$. $\mathbf{A}(\mathbf{x})$ and $\mathbf{B}(\mathbf{x})$ are the matrices which can be constructed according to the linear basis and the weight function. $\mathbf{A}(\mathbf{x})$ is called the weighted moment matrix defined by

$$\mathbf{A}(\mathbf{x}) = \sum_{I=1}^{n} \tilde{w}(\mathbf{x} - \mathbf{x}_I)\mathbf{p}(\mathbf{x}_I)\mathbf{p}^{\mathrm{T}}(\mathbf{x}_I) \tag{6}$$

and the matrix $\mathbf{B}(\mathbf{x})$ is defined as

$$\mathbf{B}(\mathbf{x}) = [\tilde{w}(\mathbf{x} - \mathbf{x}_1)\mathbf{p}(\mathbf{x}_1), \tilde{w}(\mathbf{x} - \mathbf{x}_2)\mathbf{p}(\mathbf{x}_2), ..., \tilde{w}(\mathbf{x} - \mathbf{x}_n)\mathbf{p}(\mathbf{x}_n)] \tag{7}$$

Solving Equation (5) for $\mathbf{a}(\mathbf{x})$ leads to

$$\mathbf{a}(\mathbf{x}) = \mathbf{A}^{-1}(\mathbf{x})\mathbf{B}(\mathbf{x})\mathbf{u} \tag{8}$$

Substituting the above equation back into Equation (1), we have the following the MLS approximant

$$u^h(x) = \sum_{I=1}^{n} N_I(x)u_I = \mathbf{N}(x)\mathbf{u} \tag{9}$$

where $\mathbf{N}(x)$ is the vector of MLS shape functions related to the n nodes in the local support domain of the point $\mathbf{x}$. The shape function $N_I(x)$ associated with node I at point x can be written as

$$N_I(x) = \mathbf{p}^{\mathrm{T}}(x)\left(\mathbf{A}(x)\right)^{-1}\mathbf{B}_I(x) \tag{10}$$

The partial derivative of the shape function is expressed as follows:

$$N_{I,x}(x) = \mathbf{p}^{\mathrm{T}}_{,x}(x)\mathbf{A}^{-1}(x)\mathbf{B}_I(x) + \mathbf{p}^{\mathrm{T}}(x)(\mathbf{A}^{-1}(x))_{,x}\mathbf{B}_I(x) + \mathbf{p}^{\mathrm{T}}(x)\mathbf{A}^{-1}(x)\mathbf{B}_{I,x}(x) \tag{11}$$

where

$$\mathbf{B}_{I,x}(x) = \frac{d\tilde{w}}{dx}(x - x_I)\,\mathbf{p}(x_I) \tag{12}$$

$$(\mathbf{A}(x))^{-1}_{,x} = -\mathbf{A}^{-1}(x)\mathbf{A}(x)_{,x}\mathbf{A}^{-1}(x) \tag{13}$$

where

$$\mathbf{A}_{,x}(x) = \sum_{I=1}^{n} \frac{d\tilde{w}}{dx}(x - x_I)\mathbf{p}(x_I)\mathbf{p}^{\mathrm{T}}(x_I) \tag{14}$$

The matrix $\mathbf{A}(x)$ is often referred to the moment matrix of size $m \times m$. It can be seen that this matrix must be inverted wherever the MLS shape functions are to be evaluated. Considering computational cost and the possibility of moment matrix singularity, a more efficient numerical scheme involving the LU decomposition can refer to the work of [Dolbow and Belytscko (1998)].

The MLS shape functions have the following properties:

(1) Linear consistency due to the linear basis k=1 used. The consistency condition is closely related to the completeness and reproducibility of the approximation. The lowest order form of MLS shape functions is the well-known Shepard function.

(2) Partition of unity, because the constant term is included in the basis.

(3) The desirable continuity of the approximation inherited from the weigh function of high continuity.

(4) The MLS shape function lacks of the Kronecker delta function property, as there is no guarantee that the smooth curve or surface via the least square fitting will pass through the nodes.

As aforementioned, in MLS approximations, each node is associated with a compactly supported non-negative weight function. One of the major advantages of MLS approximation is it can inherit the continuity of the weight function. A lower order polynomial basis can be used to generate higher continuous approximations by choosing a proper weight function, and so the weight function plays an important role in the performance of meshless approximations. Many functions can act as the weight functions provided that they can satisfy certain conditions [Lancaster and Salkauskas (1981)], such as continuous and derivable functions that are non-negative and compactly supported over the local domain, a normality (unity) property, a monotonically decreasing function, and Dirac delta function behavior. The condition of non-negative and compact support is crucial for the selection of weight function, as it enables the approximation to be generated via a local representation of window wavelets. The normality condition may be used to assure consistency of the discrete form of the approximation.

In terms of the above selection criteria, the commonly used weight functions for MLS approximations include the exponential, the cubic spline and the quartic spline functions. This work employs the cubic spline weight function with rectangle influence domain. The weight function and its derivative are written as a function of the normalized radius Υ[Dolbow and Belytscko (1998)], respectively,

as

$$\tilde{w}(x-x_I) = w(\Upsilon) = \begin{cases} \frac{2}{3} - 4\Upsilon^2 + 4\Upsilon^3, & \text{for } \Upsilon \le \frac{1}{2} \\ 0, & \text{for } \Upsilon > 1 \\ \frac{4}{3} - 4\Upsilon + 4\Upsilon^2 - \frac{4}{3}\Upsilon^3, & \text{for } \frac{1}{2} < \Upsilon \le 1 \end{cases} \tag{15}$$

$$\frac{d\tilde{w}_I}{dx} = \frac{d\tilde{w}_I}{d\Upsilon}\frac{d\Upsilon}{dx} = \begin{cases} (-8\Upsilon + 12\Upsilon^2) sign(x-x_I), & \text{for } \Upsilon \le \frac{1}{2} \\ 0, & \text{for } \Upsilon > 1 \\ (-4 + 8\Upsilon - 4\Upsilon^2) sign(x-x_I), & \text{for } \frac{1}{2} < \Upsilon \le 1 \end{cases} \tag{16}$$

It is noted that the spatial derivative of the weight function is necessary for the evaluation of the spatial derivative of the matrices **A** and **B**. This first-order derivative is continuous over the entire domain. By far we have obtained the MLS shape functions for meshless approximations of the displacement.

3 Level set model using MLS shape functions

As aforementioned, in most of current level set methods, the design boundary is implicitly represented by embedding it into the zero level-sets of a higher-dimensional level set surface (e.g. 2D boundary to 3D surface) [Osher and Sethian (1988); Sethian (1999); Osher and Fedkiw (2002)]. The level set optimization is actually a process of shape variations but able to achieve topological changes via boundary merging and breaking simultaneously. This process leads to an integrated shape and topology optimization with clear medium interfaces in distinct and smooth state. It is noted that the level set function itself is a mathematically only scalar function with Lipschitz continuity, without any physical meanings to mechanics problems [Luo, Zhang and Wang (2012)].

In this study, the level set function Φ is defined over a fixed reference domain **D**, a bounded open set including all the admissible shapes of the design domain $\Omega(\Omega \subset D)$. For instance, the boundary representation scheme for a 2D structure ($d = 2$) is illustrated by embedding it into a 3D level set surface at its zero level set as follows (Figure 1):

$$\begin{cases} \Phi(\mathbf{x}) < 0 \Leftrightarrow \forall \mathbf{x} \in \Omega \backslash \partial\Omega (\text{void}) \\ \Phi(\mathbf{x}) = 0 \Leftrightarrow \forall \mathbf{x} \in \partial\Omega \cap D (\text{boundary}) \\ \Phi(\mathbf{x}) > 0 \Leftrightarrow \forall \mathbf{x} \in D \backslash \Omega (\text{material}) \end{cases} \tag{17}$$

To enable the dynamic process, introducing the pseudo-time t into the level set function $\Phi(\mathbf{x})$ leads to the following first-order Hamilton-Jacobi PDE by differentiating $\Phi(\mathbf{x}(t),t) = 0$ on both sides with respect to the pseudo-time t [Sethian

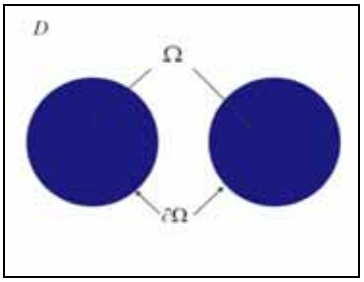

(a) 2D boundary at zero level set

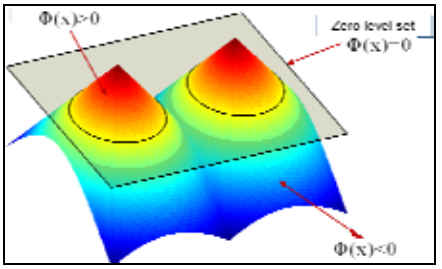

(b) 3D level set surface

Figure 1: Implicit level set representation at zero level set

(1999); Osher and Fedkiw (2002)]:

$$\frac{\partial \Phi(\mathbf{x},t)}{\partial t} + \mathbf{v}_{\mathrm{n}} |\nabla \Phi| = 0,\ \Phi(\mathbf{x},0) = \Phi_0(\mathbf{x}) \tag{18}$$

The normal velocity is expressed as follows:

$$\mathbf{v}_{\mathrm{n}} = \mathbf{v} \cdot \mathbf{n} = \mathbf{v} \cdot \left(\frac{\nabla \Phi}{|\nabla \Phi|} \right) = \frac{d\mathbf{x}}{dt} \left(\frac{\nabla \Phi}{\sqrt{\nabla \Phi \cdot \nabla \Phi}} \right) \tag{19}$$

Hence, moving boundary $\Gamma = \{\mathbf{x} | \Phi(\mathbf{x}) = \mathrm{C}\}$ along normal direction $\mathbf{n}$is equivalent to advancing the level set function Φ by solving the Hamilton-Jacobi PDE with appropriate numerical schemes. In most conventional level set methods [Wang, Wang and Guo (2003); Allaire, Jouve and Toader (2004)], the motion of the discrete level set function is governed by a process of solving the Hamilton-Jacobi PDEs on a fixed Eulerian rectilinear grids, and the velocity field in the Equation (22) is generally determined using the shape derivative analysis [Sokolowski, and Zolesio (1992)]. Since a general analytical form for the level set function is usually unknown, in conventional level set methods, explicit schemes are indispensable to enable the propagation of the discrete level set function in time.

However, as above described, numerical difficulties in conventional level set methods limit the further application of the level set methods to more advanced topology optimization problems [Sethian (1999); Osher and Fedkiw (2002)], the CFL time-marching step condition is required to be satisfied to ensure numerical stability in terms of the minimal size of a set of spatial meshes. The periodically applied re-initializations are included to maintain a regular shape of the level set surface. The unshaped level set function will influence the calculation of the derivatives and the speed of convergence, as a too step or flat level set surface will usually be developed due to the unwanted dissipation of the front.

With the MSL meshless approximation, the discrete level set surface Φ^h can be parameterized with the MLS shape functions $\mathbf{N}(x)$ and the level set nodal values $\phi(t)$ as follows:

$$\Phi^h(x,t) = \mathbf{p}^{\mathbf{T}}(\mathbf{x})\mathbf{a}(t) = \mathbf{N}(x)\phi(t) = \sum_{i=1}^{n} N_i(x)\phi_i(t) \tag{20}$$

The level set model is reshaped by substituting (24) into the original level set equation as

$$\mathbf{N}(\mathbf{x})^{\mathrm{T}}\dot{\phi}(t) - \mathbf{v_n}\left|\left(\nabla\mathbf{N}(\mathbf{x})\right)^{\mathrm{T}}\phi(t)\right| = 0 \tag{21}$$

Then $\mathbf{v_n}$ is now directly expressed as

$$\mathbf{v_n} = \frac{\mathbf{N}(\mathbf{x})^{\mathrm{T}}}{\left|\left(\nabla\mathbf{N}(x)\right)^{\mathrm{T}}\phi(t)\right|}\dot{\phi}(t) = \frac{1}{|\nabla\Phi|}\mathbf{N}(\mathbf{x})^{\mathrm{T}}\dot{\phi}(t), \text{ where } \dot{\phi}(t) = \frac{d\phi(t)}{dt} \tag{22}$$

In this way, if we suppose that the set of scattered nodes are fixed spatially in the design domain during the optimization, the original more difficult time-space Hamilton-Jacobi PDE is uncoupled into a set of ordinary differential equations, in which the discrete level set values are temporal only. Accordingly, the original more difficult shape and topology optimization is then transformed into a relatively easier size optimization, to which more efficient optimization algorithms can be applied in finding the discrete level set nodal values iteratively.

4 Meshless level-set method for geometrically nonlinear structures

In this study, the nonlinear effect as large displacements in nonlinear strain displacement is considered, under the assumption that the material is subjected to small strains. Since the initial level set function is defined with undeformed fixed reference domain, the Total Lagrange formulation [Bathe (1996)] is a natural choice for the geometrically nonlinear analysis.

For elastic solids of geometrical nonlinearity, embedding the implicit design boundary into the level set function, the variational form of the equilibrium equations can be obtained based on the principle of virtual work. Let the test function be the variational term $\delta u \in \mathbf{U}$ of the trial function $u \in \mathbf{U}$, in terms of the integration by parts and the divergence theorem, the corresponding weak formulation of the equilibrium equation [Bathe (1996)] can be expressed by

$$\int_D S_{ij}(u)\delta\varepsilon_{ij}(u;\delta u)H(\Phi)d\Omega = \int_D b_i\delta u_i H(\Phi)d\Omega + \int_{\partial D_\Gamma} t_i\delta u_i d\Gamma \tag{23}$$

Here u and δu are the trial and virtual displacement vectors, respectively, belonging to the same space $\mathbf{U}$ spanned by the kinematically admissible set of displacements. S_{ij} is the second Piola-Kirchhoff symmetrical stress tensor, and $\delta\varepsilon_{ij}$ is the virtual Green-Lagrange strain tensor. Ω and D are the design and reference design domain, respectively. $\partial D = \partial D_\Gamma \cup \partial D_u$ consists of the Neumann ∂D_Γ and Dirichlet ∂D_u boundaries. b and t are externally applied body force and boundary traction. $H(\Phi)$ and $\delta(\Phi)$ represent the Heaviside function and the corresponding Delta function, respectively [Wang, Wang and Guo (2003); Allaire, Jouve and Toader (2004)].

As aforementioned, the MLS approximation doesn't possess the Kronecker delta function property, and this study employs the penalty function method [Atluri and Shen (2002); Gu and Liu (2005)] to handle essential boundary conditions. With the total Lagrangian formulation (T.L.) referring to the initial configuration at $t = 0$, the equilibrium equation corresponding to the configuration at time $t + \Delta t$ can be expressed in the notations of internal energy and external virtual work as

$$\int_{0_D} {}_0^{t+\Delta t}S_{ij}(u)\delta\left({}_0^{t+\Delta t}\varepsilon_{ij}(u;\delta u)\right)H(\Phi)d\Omega + \alpha\int_{0_{\partial D_u}}\delta u_i^T(u_i - u_{i0})d\Gamma = {}^{t+\Delta t}a_\Phi(u,\delta u)$$

$${}^{t+\Delta t}l_\Phi(\delta u) = \int_{0_D} {}_0^{t+\Delta t}b_i\delta u_i H(\Phi)d\Omega + \int_{0_{\partial D_\Gamma}} {}_0^{t+\Delta t}t_i\delta u_i d\Gamma \tag{24}$$

where ${}^0\Omega$ and ${}^0D$ are the design and reference domain, respectively.

Using the incremental scheme [Bathe (1996)], the second Piola-Kirchhoff stress and Green-Lagrange strain tensor ε are defined by

$${}_0^{t+\Delta t}S_{ij} = {}_0^tS_{ij} + {}_0S_{ij} \tag{25}$$

$${}_0^{t+\Delta t}\varepsilon_{ij} = {}_0^t\varepsilon_{ij} + {}_0\varepsilon_{ij} \tag{26}$$

Here the first terms ${}_0^tS_{ij}$ and ${}_0^t\varepsilon_{ij}$ are known, and the first terms ${}_0S_{ij}$ and ${}_0\varepsilon_{ij}$ are the incremental of the Kirchhoff stress and the Green strain with respect to the initial configuration. So the virtual Green-Lagrange strain tensor is given by

$$\delta\left({}_0^{t+\Delta t}\varepsilon_{ij}\right) = \delta\left({}_0\varepsilon_{ij}\right) \tag{27}$$

The Green strain vector ${}_0\varepsilon_{ij}$ can be further written as

$${}_0\varepsilon_{ij} = {}_0e_{ij} + {}_0\eta_{ij} \tag{28}$$

where ${}_0e_{ij}$ and ${}_0\eta_{ij}$ are the incremental terms of the linear strain and nonlinear strain, which can be defined, respectively, as follows:

$${}_0e_{ij} = ({}_0u_{i,j} + {}_0u_{j,i})/2 + ({}_0^tu_{k,i}{}_0u_{k,j} + {}_0u_{k,i}{}_0^tu_{k,j})/2 \tag{29}$$

$$ {}_0\eta_{ij} = ({}_0u_{k,i0}u_{k,j})/2 \tag{30} $$

In this way, the equilibrium equation with the T.L. formulation can be re-defined as

$$ \int_{{}_0D} \left({}_0S_{ij}\delta_0\varepsilon_{ij} + {}^t_0S_{ij}\delta_0 e_{ij} + {}_0S_{ij}\delta_0\eta_{ij}\right)H(\Phi)d\Omega + \alpha\int_{{}_0D}\delta u_i^T(u_i-u_{i0})\delta(\Phi)\left|\nabla\Phi\right|d\Omega = {}^{t+\Delta t}\mathrm{W}_\Phi $$

$$ {}^{t+\Delta t}\mathrm{W}_\Phi = \int_{{}_0D}{}^{t+\Delta t}_0 b_i\delta u_i H(\Phi)d\Omega + \int_{{}_0D}{}^{t+\Delta t}_0 t_i\delta u_i\delta(\Phi)\left|\nabla\Phi\right|d\Omega \tag{31} $$

For large-deformation under the assumption of small strain, the constitutive relation with respect to the initial configuration can be approximately expressed via the material elasticity tensor D_{ijkl} as

$$ {}_0S_{ij}(u) = {}_0D_{ijkl0}\varepsilon_{kl} \tag{32} $$

It is noted that the second Piola-Kirchhoff symmetrical stress tensor ${}_0S_{ij}$, rather than the original nonsymmetrical Green-Lagrange stress tensor, and the Green-Lagrange strain tensor ${}_0\varepsilon_{kl}$ are used.

Substituting the above linearized constitutive equation into Equation (31), the first term is given by

$$ \int_{{}_0D}({}_0S_{ij}\delta_0\varepsilon_{ij})H(\Phi)d\Omega = \int_{{}_0D}{}_0D_{ijkl}({}_0e_{kl}+{}_0\eta_{kl})(\delta_0 e_{ij}+\delta_0\eta_{ij})H(\Phi)d\Omega \tag{33} $$

Eliminating the terms related to the nonlinear strain ${}_0\eta_{ij}$, and the linearized equilibrium equation is

$$ \int_{{}_0D}{}_0D_{ijkl0}e_{kl}\delta({}_0e_{ij})H(\Phi)d\Omega + \int_{{}_0D}{}^t_0S_{ij}\delta({}_0\eta_{ij})H(\Phi)d\Omega + \alpha\int_{{}_0D}\delta u_i^T(u_i-u_{i0})\delta(\Phi)\left|\nabla\Phi\right|d\Omega = {}^{t+\Delta t}\mathrm{W}_\Phi - \int_{{}_0D}{}^t_0S_{ij}\delta({}_0e_{ij})H(\Phi)d\Omega \tag{34} $$

Define a linearized bilinear functional:

$$ \tilde{\mathbf{a}}_\Phi = \int_{{}_0D}{}_0D_{ijkl0}e_{kl}\delta({}_0e_{ij})H(\Phi)d\Omega + \int_{{}_0D}{}^t_0S_{ij}\delta({}_0\eta_{ij})H(\Phi)d\Omega + \alpha\int_{{}_0\partial D_u}\delta u_i^T(u_i-u_{i0})d\Gamma \tag{35} $$

and a linearized load form:

$$ \tilde{\mathbf{l}}_\Phi = {}^{t+\Delta t}\mathrm{W}_\Phi - \int_{{}_0D}{}^t_0S_{ij}\delta({}_0e_{ij})H(\Phi)d\Omega \tag{36} $$

Thus the equilibrium equation with the linearized terms at the current configuration is re-defined by

$$ {}^{t}_{0}\mathbf{R} = \tilde{\mathbf{a}}_{\Phi}(u, \delta u, u_i) - \tilde{\mathbf{l}}_{\Phi}(u, \delta u) \approx 0 \tag{37} $$

where ${}^{t}_{0}\mathbf{R}$ denotes the residual load vector at the current configuration, due to the unbalanced stress caused by the linearization of the equilibrium equation involving the displacement increment $\mathbf{u}_i$.

In numerical implementation, the modified Newton-Raphson iteration scheme [Bathe (1996)] is used to balance the stress caused by the linearization until ${}^{t}_{0}\mathbf{R}$ is small enough. With the MLS shape function $\mathbf{N}(\mathrm{x})$, the current nodal displacement vector, the related nodal point forces, and the tangential stiffness matrix for the next iteration can be obtained based on u_i.

Substituting $\mathbf{N}(\mathrm{x})$ into u_i yields the following meshless approximations:

$$ {}^{t+\Delta t}u^h(x) = \sum_{i=1}^{n} {}^{t}N_i(x)\,{}^{t}u_i = {}^{t}\mathbf{N}(x)\,{}^{t}\mathbf{u}_i^T, \tag{38} $$

where $\mathbf{u}_i^T = [u_1, u_1, ..., u_n]$.

where $\mathbf{N}(x)$ is the MLS shape functions already obtained previously. $\mathbf{u}_i$ is the vector of the nodal displacement incremental. n is the number of the nodes in the support domain of the point x to construct MLS shape functions.

With the meshless MLS approximations, the linearized T.L. formulation of the equilibrium equation can be re-expressed in the matrix form as:

$$ {}^{t}_{0}\mathbf{R} = ({}^{t}_{0}\mathbf{K}_{L0} + {}^{t}_{0}\mathbf{K}_{L1} + {}^{t}_{0}\mathbf{K}_{NL} + {}^{t}_{0}\mathbf{K}_{P})\mathbf{u}_i - ({}^{t+\Delta t}\mathbf{W} - {}^{t}_{0}\mathbf{F}) \approx 0 \tag{39} $$

where $\mathbf{u}_i$ is the nodal displacement vector consisting of the increments. From this equation, it can be seen that the tangent stiffness matrix is composed of four different matrix terms. So the four matrices, and the external force vector, as well as the nodal force vector are defined as follows, respectively

$$ {}^{t}_{0}\mathbf{K}_{L0} = \int_{{}_0D} {}^{t}_{0}\mathbf{B}^T_{L_0 0}\mathbf{D}\,{}^{t}_{0}\mathbf{B}_{L_0} H(\Phi) d\Omega \tag{40} $$

$$ {}^{t}_{0}\mathbf{K}_{L1} = \int_{{}_0D} \left({}^{t}_{0}\mathbf{B}^T_{L_0 0}\mathbf{D}\,{}^{t}_{0}\mathbf{B}_{L_1} + {}^{t}_{0}\mathbf{B}^T_{L_1 0}\mathbf{D}\,{}^{t}_{0}\mathbf{B}_{L_0} + {}^{t}_{0}\mathbf{B}^T_{L_1 0}\mathbf{D}\,{}^{t}_{0}\mathbf{B}_{L_1}\right) H(\Phi) d\Omega \tag{41} $$

$$ {}^{t}_{0}\mathbf{K}_{NL} = \int_{{}_0D} {}^{t}_{0}\mathbf{B}^T_{NL 0}\mathbf{S}\,{}^{t}_{0}\mathbf{B}_{NL} H(\Phi) d\Omega \tag{42} $$

$$ {}^{t}_{0}\mathbf{K}_{P} = \alpha \int_{{}_0\partial D_u} {}^{t}_{0}\mathbf{N}(x)^T\,{}_0\mathbf{Z}\,{}^{t}_{0}\mathbf{N}(x) H(\Phi) d\Omega \tag{43} $$

$$^{t+\Delta t}\mathbf{W} = \int_{_0D} {}^{t}_{0}\mathbf{N}(x)^{t+\Delta t}_{0}\mathbf{b}H(\Phi)d\Omega + \int_{_0\partial D_t} {}^{t}_{0}\mathbf{N}(x)^{t+\Delta t}_{0}\mathbf{t}d\Gamma + \alpha \int_{_0\partial D_u} {}^{t}_{0}\mathbf{N}(x)^{T}\,{}_0\mathbf{Z}^{t}_{0}\mathbf{u}_0 d\Gamma \tag{44}$$

$${}^{t}_{0}\mathbf{F}_{NL} = \int_{_0D} \left({}^{t}_{0}\mathbf{B}^{T}_{L_0} + {}^{t}_{0}\mathbf{B}^{T}_{L_1}\right) {}_0\bar{\mathbf{S}}H(\Phi)d\Omega \tag{45}$$

In the above equations, ${}_0\mathbf{D}$ represents the practical material elasticity property matrix. ${}^{t}_{0}\mathbf{K}_{L0}$ is the matrix corresponding to the small displacement, called small-displacement matrix, and ${}^{t}_{0}\mathbf{K}_{L1}$ is the matrix caused by the displacement ${}^{t}_{0}u_i$ at the initial configuration, in the name of initial displacement or large-displacement matrix. ${}^{t}_{0}\mathbf{B}_{L_0}$ is the small deformation strain-displacement matrix, which is related to the first part $({}_0u_{i,j} + {}_0u_{j,i})/2$ in the linear strain ${}_0e_{ij}$, while ${}^{t}_{0}\mathbf{B}_{L_1}$ is the strain-displacement matrix corresponding to the second part $({}^{t}_{0}u_{k,i}{}_0u_{k,j} + {}_0u_{k,i}{}^{t}_{0}u_{k,j})/2$ in the linear strain ${}_0e_{ij}$. ${}^{t}_{0}\mathbf{K}_{NL}$ defines a tangent stiffness matrix arising from the stress matrix ${}_0\mathbf{S}$ at the initial configuration, named geometric matrix or initial stress matrix. ${}^{t}_{0}\mathbf{K}_{NL}$ is related to the strain-displacement matrix ${}^{t}_{0}\mathbf{B}_{NL}$ of the non-linear strain ${}_0\eta_{ij}$. ${}^{t}_{0}\mathbf{K}_{P}$ is the matrix term caused by the penalty function in order to enforce the essential boundary condition in MLS meshless approximation, in which ${}^{t}_{0}\mathbf{N}(x)$ is the MLS shape function. ${}_0\mathbf{Z}$ is the matrix consisting of two entries for displacement constraint in two different directions in 2D Cartesian coordinates. ${}_0\mathbf{S}$ and ${}_0\bar{\mathbf{S}}$ are used to denote the matrix and the vector of the second Piola-Kirchhoff stress, respectively.

So in this way the MLS meshless approximation of Galerkin weak-form can be used to establish a set of discretized system equations for the displacement vector of the trial function. The strain at any point can also be obtained using the derivatives of the MLS shape functions and the nodal displacements. The penalty method can lead to a positive definite system matrix, as it enforces the essential boundary condition without increasing the size of the system equations.

5 Optimal design of compliant mechanisms

In this section, the optimal design of compliant mechanisms is mathematically established to maximize the output displacement under two specified constraints. The differentiability of the meshless level set approximations allows the rigorous shape sensitivity analysis for geometrically nonlinear structures without losing the generality [Kwak and Cho (2005)]. For numerical simplicity, the optimization problem is considered here only with single input and a single output.

5.1 Mathematical formulation

The design of compliant mechanisms concerned in this study is illustrated as Figure 2. An artificial spring model [Sigmund (1997)] is amounted at the output port to model the clearance and simulate the reaction force between the workpiece and the mechanical piece. The spring model refers to an artificial spring with a pre-known stiffness $k = c$ attached in the expected output direction. For the topology optimization of compliant mechanisms, there are many objective functions under the assumption of linear elasticity. However, the linearity assumption may not be properly applied to compliant mechanisms involving geometrical nonlinearity for various reasons [Pedersen, Buhl and Sigmund (2001); Luo, Zhang, Ji and Wu (2012)].

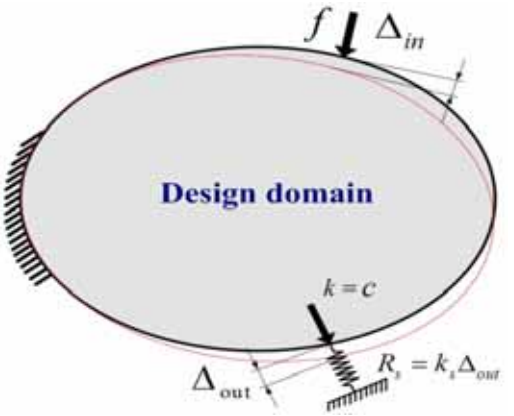

Figure 2: Model of compliant mechanisms

By far the widely used objective function to capture the large-formation compliant mechanisms is the displacement output or the equivalent forms [Bruns and Tortorelli (2001); Cho and Kwak (2006); Luo, Zhang, Ji and Wu (2012)]. So in this study the displacement output is used as the objective function under two constraints. The level-set optimization problem is now formulated as follows

$$\begin{cases} \underset{(\Phi)}{\text{Minimize}} : u_{out} \\ \text{Subject to:} \begin{cases} u_{\text{in}} - u_{in}^{*} \le 0, \\ \int_D H(\Phi) d\Omega - V^{*} \le 0, \\ \tilde{\mathbf{a}}_{\Phi}(u, \delta u, u_i) = \tilde{\mathbf{l}}_{\Phi}(u, \delta u), \forall \delta u \in \mathbf{U} \end{cases} \end{cases} \tag{46}$$

where u_{out} is defined as the objective function, and u_{in} refers to the displacement

occurred at the input position. The first constraint is applied to restrain the maximal displacement input u_{in}^{*} and to prevent excessive deformation and stress level inside the mechanism, so as to avoid convergence difficulties [Sigmund (1997)]. The second constraint is used to restrict the allowable material usage V^{*} in order to generate "truss-type" structural segments in the mechanism.

5.2 Design sensitivity analysis

The design sensitivity is performed to enable the dynamic boundary evolvement of the mechanism by using both the concept of shape derivative [Sokolowski and Zolesio (1992)] and the procedure of adjoint sensitivity analysis method.

First, the displacement υ_i for the ith degree of freedom is defined by

$$\upsilon_i = \mathbf{L}^{\mathrm{T}}\mathbf{U} \tag{47}$$

where $\mathbf{L}$ is a unit load vector consisting of an entry of $L_i = 1$ at position i, and the rest of the entries are zero. $\mathbf{U}$ is the displacement vector produced by the applied load $\mathbf{F}$ at the input port, which can be obtained using MLS meshless approximation.

Introducing a vector of Lagranian multiplier λ, the original objective function is augmented as a new objective without changing anything by adding the term $\lambda^{\mathrm{T}}\mathbf{R}$ related to the residual term $\mathbf{R}$

$$u_i = \mathbf{L}^{\mathrm{T}}\mathbf{U} + \lambda^{\mathrm{T}}\mathbf{R} \tag{48}$$

and the design sensitivity of the augmented objective function can be obtained as

$$\frac{d\upsilon_{out}}{d\alpha_i} = (\mathbf{L}^{\mathrm{T}} + \lambda^{\mathrm{T}}\frac{\partial \mathbf{R}}{\partial \mathbf{U}})\frac{d\mathbf{U}}{d\alpha_i}\mathbf{L} + \lambda^{\mathrm{T}}\frac{\partial \mathbf{R}}{\partial \alpha_i} \tag{49}$$

By setting the displacement vector λ to be the solution of the following equation

$$\mathbf{K}\lambda = -\mathbf{L} \tag{50}$$

where $\mathbf{K}$ is the tangential stiffness matrix which has been factorized from the primary MLS meshless analysis, which makes the numerical problem with a reasonable computational expense. Due to the Equation (48) is always satisfied at the equilibrium state, the term related to $\mathbf{R}$ will remain zero regardless of the choice of the displacement vector λ. So, the sensitivity can be simplified as

$$\frac{d\upsilon_{out}}{d\alpha_i} = \lambda^{\mathrm{T}}\frac{\partial \mathbf{R}}{\partial \alpha_i} \tag{51}$$

Now, our major task is to find out the sensitivity of the residual with respect to the variation of the design variables. It is noted that the residual **R** can be re-written in a general functional form as

$$\mathbf{R}_{\Phi}({}_0^{t+\Delta t}u) = \int_{{}_0D} \Re({}_0^{t+\Delta t}u) H(\Phi) d^0\Omega \tag{52}$$

Its shape derivative at configuration $(t+\Delta t)$ can be found by following the same procedure as that in the relevant references [Wang, Wang and Guo (2003); Allaire, Jouve and Toader (2004); Luo, Tong, and Kang (2009)].

$$\frac{\partial \mathbf{R}_{\Phi}({}_0^{t+\Delta t}u)}{\partial t} = \int_{{}_0D} \rho_{\Phi}({}_0^{t+\Delta t}u, w)\delta(\Phi)|\nabla\Phi|\,\mathbf{v_n} d\Omega \tag{53}$$

Recalling the normal velocity vector $\mathbf{v_n}$ defined in Equation (23), and substituting it into the above Equation (58), the shape derivative for the residual load of geometrically nonlinear structures is

$$\frac{\partial \mathbf{R}_{\Phi}({}_0^{t+\Delta t}u)}{\partial t} = \sum_{i=1}^{n} \left(\int_{{}_0D} \rho_{\Phi}({}_0^{t+\Delta t}u, w)\delta(\Phi) N_i(x) d\Omega \right) \dot{\phi}_i(t) \tag{54}$$

where ρ is the shape gradient density, which can be defined as follows

$$\rho_{\Phi}({}_0^{t+\Delta t}u, w) = \Re({}_0^{t+\Delta t}u) - D_{ijkl}\varepsilon_{kl}({}_0^{t+\Delta t}u)\delta\varepsilon_{ij}({}_0^{t+\Delta t}u; w) + {}_0^{t+\Delta t}pw$$
$$+ \left(\nabla({}_0^{t+\Delta t}\tau w) \cdot \frac{\nabla\Phi}{|\nabla\Phi|} + \left(\nabla \cdot \frac{\nabla\Phi}{|\nabla\Phi|} \right) {}_0^{t+\Delta t}\tau w \right) \tag{55}$$

On the other hand, by the chain rule, the shape derivative of the residual load is given as follows:

$$\frac{\partial \mathbf{R}_{\Phi}({}_0^{t+\Delta t}u)}{\partial t} = \sum_{i=1}^{n} \frac{d\mathbf{R}_{\Phi}({}_0^{t+\Delta t}u)}{d\phi_i} \dot{\phi}_i(t) \tag{56}$$

Thus, the design sensitivity with respect to the discrete level set nodal values can be expressed as

$$\frac{\partial \mathbf{R}_{\Phi}({}_0^{t+\Delta t}u)}{\partial \phi_i} = \int_{{}_0D} \rho_{\Phi}({}_0^{t+\Delta t}u, w, \lambda)\delta_{\nu}(\Phi) N_i(x) d\Omega \tag{57}$$

where δ_{ν} is a regularized version of the Dirac function given as follows:

$$\delta_{\nu}(\Phi(x)) = 1/\pi\nu \cdot \left(1 + \left(\frac{\Phi(x)}{\nu} \right)^2 \right) \tag{58}$$

Here ν is a real positive constant, and it is usually chosen as 2-4 times as the mesh size in terms of numerical experiences.

In the above equations, λ is the displacement vector by applying the unit load vector $\mathbf{L}$ at the output position. ϕ_i are the unknown parameters served as the design variables of the size optimization to be updated in time. It can be seen that the complaint mechanism with geometrical nonlinearity is not self-adjoint. The adjoint displacement vector w is introduced to indicate the terms dependent on design perturbations by the following equation

$$\int_{0_D} {}^{t}_{0}S_{ij}(w)\delta({}_{0}e_{ij}(w;\delta u))H(\Phi)d\Omega = \int_{0_D} \frac{\partial \Re({}^{t+\Delta t}_{0}u)}{\partial u} H(\Phi)\delta u d\Omega \tag{59}$$

where w is computationally cheap because the factorized tangential stiffness matrix has already been obtained in the prime MLS meshless subroutine.

Once getting the design sensitivities of the objective function and constraint, the rest is just a question of applying appropriate optimization algorithms to update the discrete nodal level set values in time. For the parametric optimization problem, several optimization algorithms can be used to update the design variables, including the Optimality Criteria (OC) method [Zhou and Rozvany (1991); Sigmund (2001)], mathematical programming techniques, e.g. the Method of Moving Asymptotes (MMA) [Svanberg (1987)]. In this work, the MMA algorithm is used as the optimizer.

6 Numerical Implementation of Meshless Approximations

For the MLS Galerkin meshless approximation, a background shadow cell structure, independent of the set of scattered field nodes, is required for implementing numerical quadrature of the system stiffness matrix. The system matrix is assembled by a two-step procedure: the first step is to loop over all the cells of the background mesh, and the second step is to evaluate all Gauss quadrature points (4×4=16 computational points) inside each cell. In this study (Fig. 3), a rectangular background mesh is used to implement the quadrature for numerical simplicity. Another issue in the implementation of the meshless level set method is the representation of the implicit moving boundary without remeshing for discontinuities [Allaire, Jouve and Toader (2004); Luo, Zhang, Ji and Wu (2012)]. In particular, the EFG method shows potential in handling moving boundary discontinuities in level set models.

This Section focus on the implementation of a very simple and effective scheme for evaluating the strain field in terms of discrete level set nodal values. As described previously, the discrete level set values at field nodes denotes the solid material points (Φ_I>0), and void (weak) material points (Φ_I<0), as well as the design

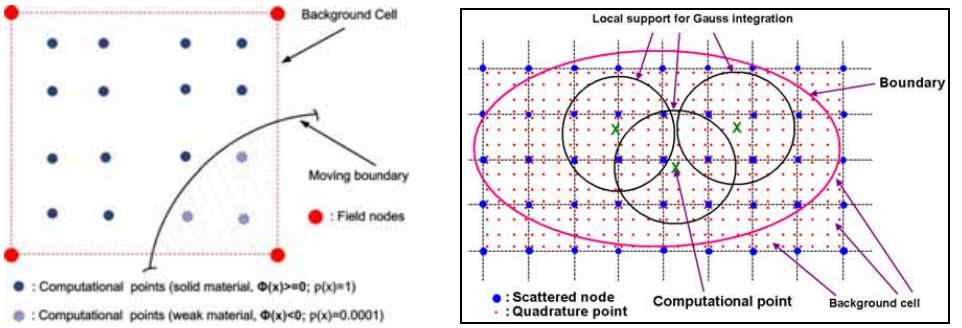

(a) (b)

Figure 3: Background cells, field nodes and quadrature/computational points

boundary where the level set nodal values are zero (Φ_I=0). So it is straightforward to get point-wise density values over the computational points in terms of the discrete level set nodal values. The field nodes can only show the relative position of different nodes, and it is difficult to describe the degree of how the boundary closes to these nodes. In practice, a relatively large number of scattered field nodes are required for an accurate material property representation, but it will greatly increase system degrees leading to a substantial increase of the computational cost.

To overcome this difficulty, the 4×4=16 quadrature (computational) points in each cell are employed on behalf of the field nodes, to describe the geometry of the moving boundaries without significantly increasing the system degree. In this way, it can directly obtain the discrete level-set point values over the quadrature points, just according to a local interpolation of the discrete level set nodal values. The major merit of this simple scheme is a direct determination of the densities at the computational points based on the discrete level set nodal values, rather than the interpolation of the field nodal densities.

After obtaining the point-wise density field over Gauss quadrature points, the Young's modulus for any computational point 'x' inside the design domain can be represented as follows:

$$E(x) = \rho(x)E_0 \tag{60}$$

where $\rho(x)$ is the practical density at 'x', and E_0 is the solid-state Young's modulus. According to the practical Young's modulus $E(x)$, it is easy to get the practical material elasticity $D(x)$. The level set function values at any quadrature point can

be determined by the local interpolation inside the cell.

$$\Phi(\mathrm{x_J}) = \sum_{S=1}^{S_J} \left[\mathbf{L}_\mathrm{S}\left(\mathrm{x_J}(r_{\mathrm{JS}})\right)\Phi_\mathrm{S}\right] \tag{61}$$

where Φ_S is the discrete level set nodal values of shadow cell S_J of the J^{th} quadrature point. $\mathbf{L}_\mathrm{S}$ is the standard Lagrange shape function. So the density at the J^{th} quadrature point can be determined in terms of $\Phi(\mathrm{x_J})$ at this point:

$$\rho(\mathrm{x_J}) = \begin{cases} 1, & \text{if } \Phi(\mathrm{x_J}) > 0 \\ 1, & \text{if } \Phi(\mathrm{x_J}) = 0 \\ 0.0001, & \text{if } \Phi(\mathrm{x_J}) < 0 \end{cases} \tag{62}$$

As aforementioned, for geometrically nonlinear structures, the system tangent stiffness matrix $\mathbf{K}$ consists of four different matrix terms, which can be obtained via the Guass quadrature, respectively, with a similar numerical procedure based on the background cells. For instance, ${}^t_0\mathbf{K}_{L_0}$ is given as

$${}^t_0\mathbf{K}_{L_0}(s,t) = \sum_{i=1}^{4}\sum_{j=1}^{4}\left\{h^t_0\mathbf{B}^T(s_i,t_j)({}^t_0\rho(s_i,t_j)\mathbf{D}_0){}^t_0\mathbf{B}(s_i,t_j)\left|{}^t_0\mathbf{J}(s_i,t_j)\right|w_i w_j\right\} \tag{63}$$

In the above equations, ρ is the corresponding density at the related Gauss point. w is the weighting factor, $\mathbf{D}_0$ represents the elasticity matrix of the full solid material properties at the quadrature points, and $\mathbf{J}$ is the Jacobin determinant. Once the system tangent stiffness matrix and the nodal displacement vector are obtained, the strain energy densities for the '**shape gradient density**' in the shape derivative analysis can also be obtained straightforwardly.

7 Numerical example: Inverter mechanism

In this section, one benchmark numerical example, inverter mechanisms, is used to demonstrate the effectiveness of the proposed meshless level set method in the design of compliant mechanisms. The level set function is initially embedded as a signed distance function, and the corresponding level set nodal values can be used to determine the initial point-wise density field. No further reinitializations are applied. The regular background cell structure is used for the numerical integration of the Galerkin weak-form. For the "artificial" material model: Young's modulus for full solid material is 200, for weak material to fill the void area is 0.2, and Poisson's ratio for all material inside the design domain is 0.3. It is noted that in topology optimization the units for the artificial material model can be defined flexibly but all the units are required to be unchanged during the design optimization.

Figure 4 is the design domain of the cantilever beam with L=30. The left side of the domain is fixed as the Dirichlet boundary while the right side is treated as a non-homogenous Neumann boundary with a concentrated force F=5 vertically applied at the center point. Only the upper half of the structure is considered in numerical procedure due to its symmetry, but the entire structural topologies will be given for exploring the whole mechanism. The objective function is to minimize the mean compliance, and the constraint is to limit the maximum material usage less than 22.5%, and the allowable input displacement is set as 6. In numerical implementation, alternatively, the maximal input displacement can also be adjusted via the input force and an artificial spring to be attached at the input port. The design domain is discretized with a set of nodes (61×31=1891), and a number of regular background cells (60×30=1800) are used only for numerical integration.

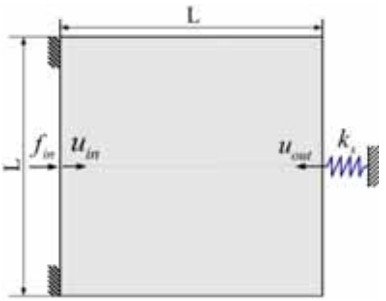

Figure 4: Design domain of compliant inverter mechanism

In the first case, an artificial spring with stiffness k_s=0.5 is mounted at the output port position to simulate the resistance from a work-piece. To limit the input displacement, the artificial spring stiffness at the input port is set to 5. The shape and topology optimization is converged after 517 iterations, and the overall displacement is maximized from -0.0214 to 0.0.4628. Figure 5 displays the topology plots of the level-set contours at the zero level set, and the corresponding topology plots of Gauss quadrature points are shown in Figure 6. It can be found that the favorable features [Osher and Sethian (1988); Sethian (1999)] of the level set-based free boundary representation scheme are well maintained, such as the concise interface and smooth boundary, merging existing holes and creating new holes to enable shape fidelities and topological flexibilities. Also we can see that the initial level set function has a relatively simple shape and topology, but it can implement more complicate shape fidelity and topology changes. The level-set based shape evolution and its topology propagation of the design boundary are actually determined by a sequence of solutions of the size optimization, which is obtained via the MLS

meshless approximations on the set of field nods. The final mechanisms are similar to those widely reported in the relevant literatures.

In Figure 6, the material density field for the computational pints can be directly determined via the interpolation of discrete nodal level set values, in which the densities for solid material points are ρ=1 (Φ>=0) and for weak material points are ρ=0.001 (Φ<0). The plots in Figure 6 are exactly align with the level-set topological contours at the zero level set, which denotes that the computational points are very suitable in describing the local details for the shape fidelity and topology changes of the moving boundaries. The topology plots for deformation are given in Figure 7 to show the effect of the large deformation of nodal field displacement effect for geometrically nonlinear structures. The more detailed discussion for large-displacement compliant mechanisms can be found in literatures, such as [Bruns and Tortorelli (2001); Pedersen, Buhl and Sigmund (2001); Luo, Zhang, Ji and Wu (2012)]. However, it is noted that the effect of geometrical nonlinearity is a nature behavior of compliant mechanisms. So, the large-displacement effect is in general required to be included, despite the finite element or the meshless numerical methods are employed in the model of compliant mechanisms.

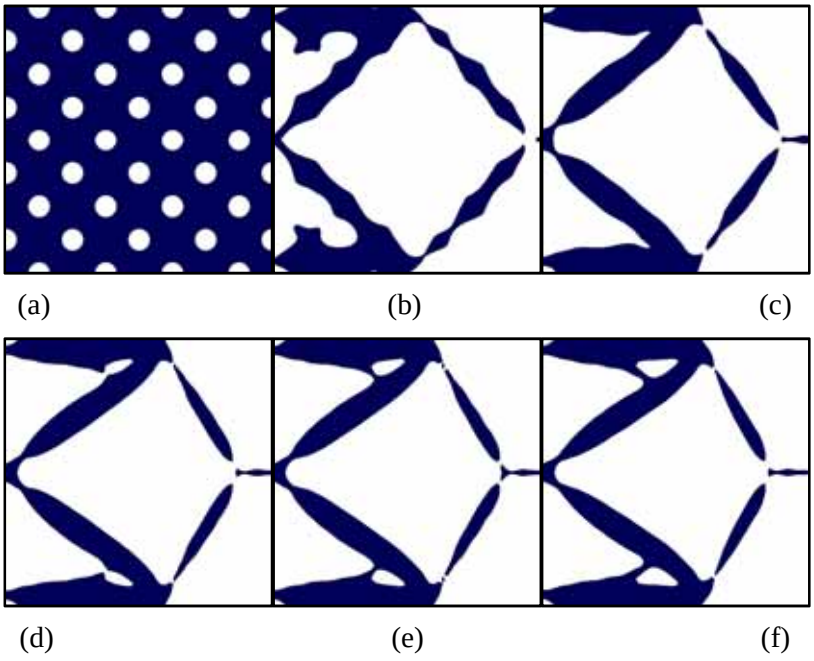

Figure 5: Topology plots of level-set contours at zero level set

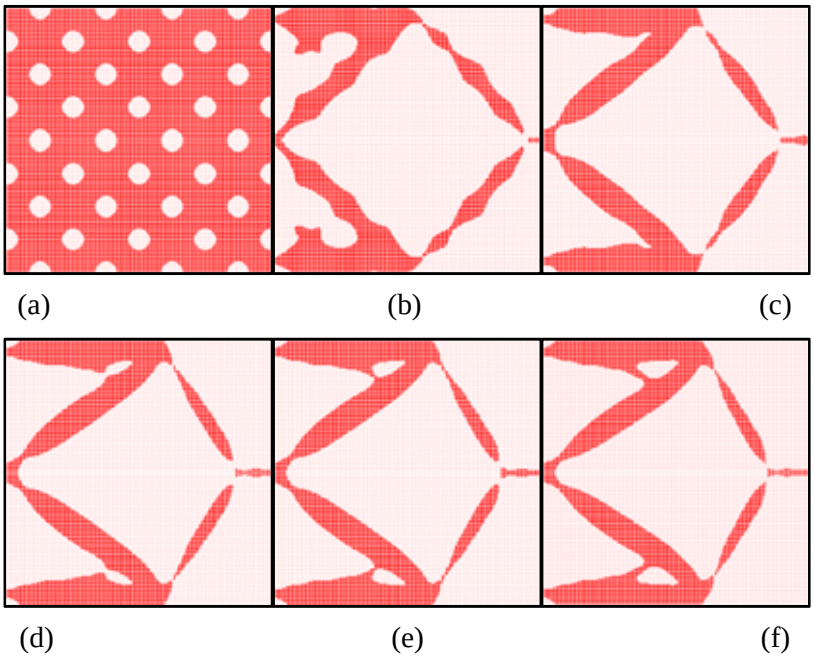

Figure 6: Topology plots of Gauss quadrature points

Figure 7 displays curves of the objective function and the volume constraint over the iterations. It can be seen that the first a small amount of iterations are mainly used to push the volume back to satisfy the constraint. Then the following iterations, less than 150 steps, are used for structural topological changes. The rest of iterations are applied to achieve shape variations, which occupies a majority of computational time of the optimization process. However, this cost is necessary to adjust the distribution of the material inside the domain to satisfy the optimal criteria. The constraint curve shows that the proposed method is mass conservative, compared to most conventional level set methods.

In the second case, an artificial spring with stiffness k_s=5 is attached at the output port position to simulate the resistance from a work-piece, the artificial spring stiffness at the input port is set to 0.5, to limit the maximal input displacement. Figure 8 shows the level-set topology contours at the zero level set, Figure 9 is the related topology plots of Gauss quadrature points, and Figure 10 is the displacement deformation for the geometrically nonlinearity effect.

With Garlerkin global weak form, it can be seen that the two typical numerical procedures in most conventional level set methods [Sethian (1999)] can be seam-

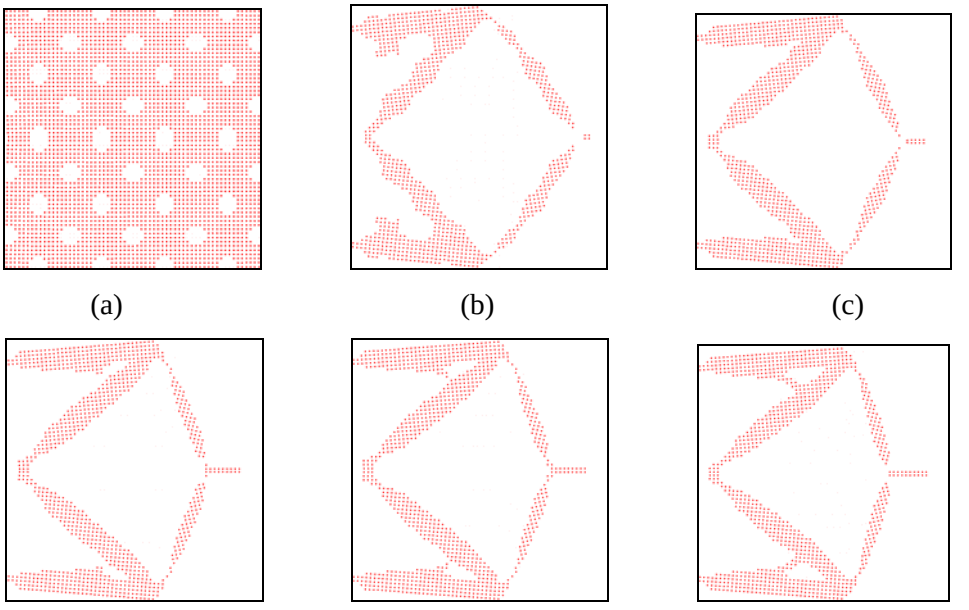

Figure 7: Topology plots of deformation for field nodal points

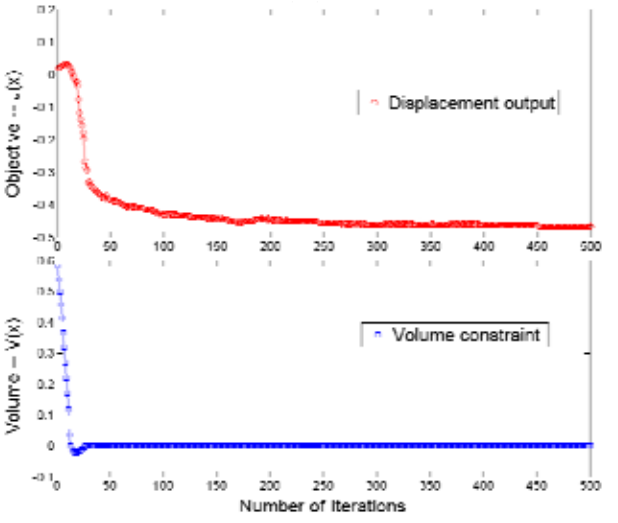

Figure 8: Curves of objective function and volume constraint

less integrated in a uniform framework, and numerical difficulties in solving the Hamilton-Jacobi PDEs can be avoided because of the parameterization of the level set function. The objective and constraint curves over the iterations are given in Figure 11. It can be found the design is converged after 521 iterations with the output displacement maximized from -0.0215 to 0.5332. The result is slightly different from the previous result due to the difference of spring stiffness, which can flexibly control the maximal displacement inputs as well as the maximal displacement outputs, to create different topological designs.

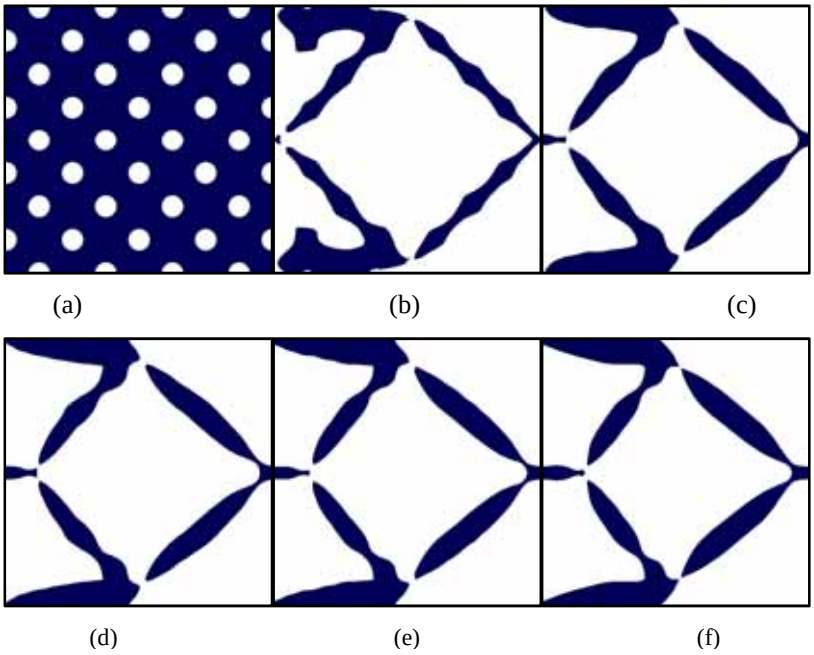

Figure 9: Topology plots of level-set contours at zero level set

In this Section, two numerical cases for a benchmark compliant mechanism have been discussed to showcase the effectiveness of the proposed meshless level set method. In both numerical cases, it is noted that the present meshless level set method cannot prevent the occurrence of the de-facto hinges in the resulting mechanisms. The de-facto hinge problem is an open topic in the topology optimization of compliant mechanisms. The further investigation for the hinge problem is out of the scope of this study. The proposed method the numerical difficulties can be avoided. The more efficient optimization algorithms in the community of the structural optimization can be directly applied. It noted that the overall computational expense is higher than the methods based on finite element methods, because the

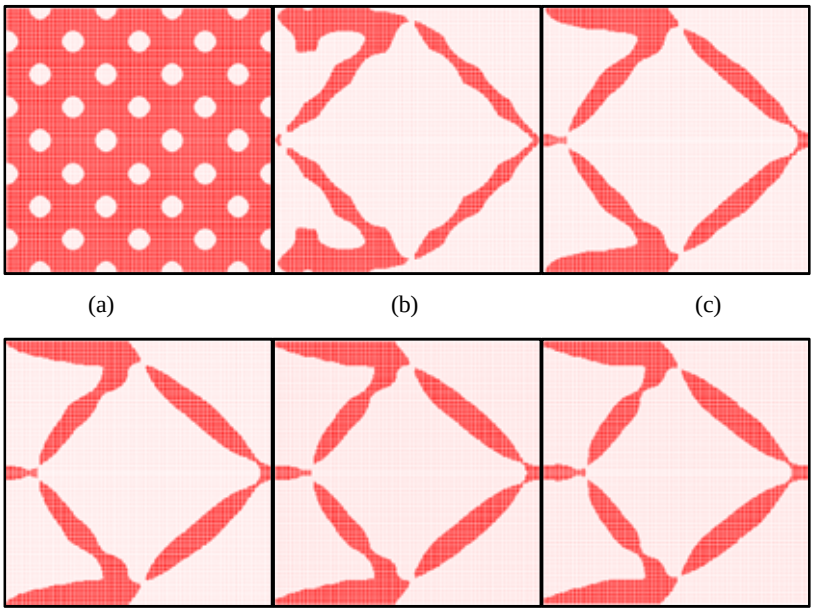

Figure 10: Topology plots of Gauss quadrature points

background shadow cells are utilized in numerical integration for the state equations. However, this study is not focused on the study of the meshless method itself. It is straightforward to incorporate the other meshless methods into the level set model for shape and topology optimization.

8 Conclusions

This study has proposed a meshless level set method for structural shape and topology optimization involving geometrical nonlinearity. The MLS shape functions are first used to implement the discrete level set function via MLS surface fitting rather than interpolation, and then to construct the meshfree function approximation with global weak form. The design problem is fully parameterized into a size optimization, without experiencing numerical difficulties in most conventional level set methods. The motion of the design boundary is just a question of transporting the discrete level set function values by finding solving the size optimization. One benchmark example of compliant mechanisms is applied to demonstrate the effectiveness of the proposed method. This study provides an extended level set method which can be applied to more advanced shape and topology optimization problems.

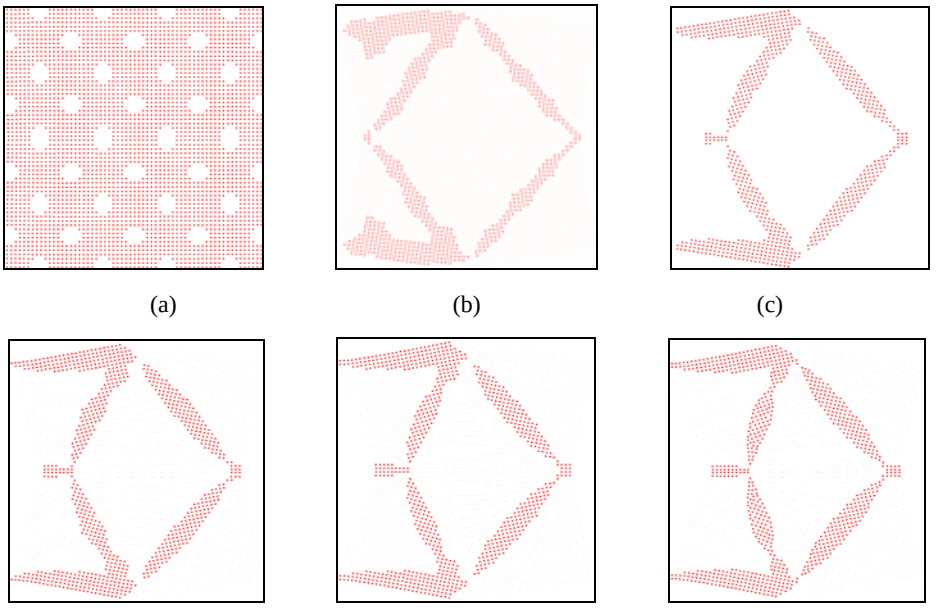

(a) (b) (c)

(d) (e) (f)

Figure 11: Topology plots of deformation for field nodal points

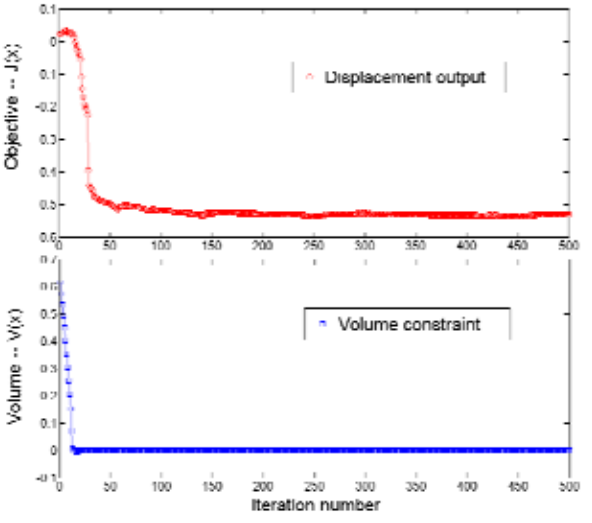

Figure 12: Curves of objective function and volume constraint

Acknowledgement: This research is supported by Chancellor's Research Fellowship (2032063, University of Technology, Sydney), Natural-Science-Foundation of China (51105229, 51175197), Open Research Foundation (GZ1007) of "State Key Lab. of Structural Analysis for Industrial Equipment", Dalian University of Technology, China, and Open Research Foundation (DMETKF2010004) of "State Key Lab. of Digital Manufacturing Equipment & Technology", Huazhong University of Science & Technology, China. The authors thank Prof. Krister Svanberg for providing his MMA codes.

References

Ananthasuresh, G.K., Howell, L.L. (2005): Mechanical design of compliant microsystems - A perspective and prospects, *Journal of Mechanical Design*, vol. 127, pp. 736-738.

Allaire, G., Jouve, F., Toader, A.M. (2004): Structural optimization using sensitivity analysis and a level-set method, *Journal of Computational Physics*, vol. 194, pp. 363-393.

Atluri S.N., Zhu T. (1998): A new meshless local Petrov-Galerkin (MLPG) approach in computational mechanics, *Computational Mechanics*, Vol. 22, pp. 117-127.

Atluri, S.N., Shen, S. (2002): The meshless local Petrov-Galerkin (MLPG) method, Tech Science Press: Encino, CA.

Bath, K.J. (1996): Finite Element Procedures. Prentice-Hall: Englewood Cliffs, NJ.

Belytschko, T., Lu, Y.Y., Gu, L. (1994): Element-free Galerkin methods, *International Journal for Numerical Methods in Engineering*, vol. 37, pp. 229-256.

Belytschko, T., Krongauz, Y., Organ, D., Fleming, M., Krysl, P. (1996): Meshless methods: an overview and recent developments, *Computer Methods in Applied Mechanics and Engineering*, vol. 139, pp. 3-47.

Bendsøe, M.P., Kikuchi, N. (1988): Generating optimal topology in structural design using a homogenization method, *Computer Methods in Applied Mechanics and Engineering*, vol. 71, pp. 197-224.

Bendsøe, M.P., Sigmund, O. (1999): Material interpolation schemes in topology optimization, *Archive of Applied Mechanics*, vol. 69, pp. 635-654.

Bendsøe, M.P., Sigmund, O. (2003): Topology optimization: Theory, Methods, and Applications, Springer, Berlin Heidelberg.

Bruns, T.E., Tortorelli, D.A. (2001): Topology optimization of nonlinear elastic structures and compliant mechanisms, *Computer Methods in Applied Mechanics*

and Engineering, vol. 190, pp. 3443-3459.

Cho, S., Kwak, J. (2006): Topology design optimization of geometrically nonlinear structures using meshfree method, *Computer Methods in Applied Mechanics and Engineering*, vol. 195, pp. 5909-5925.

Dolbow, J., Belytschko, T. (1998): An introduction to programming the meshless element free Galerkin method, *Archives of Computational Methods in Engineering*, vol. 5, pp. 207-241.

Du, Y., Luo, Z., Tian, Q. and Chen, L. (2009): Topology optimization for thermomechanical compliant actuators using meshfree methods, *Engineering Optimization*, vol. 41, pp. 753-772.

Howell, L.L. (2001): Compliant mechanisms, John Wiley & Sons, Inc., New York.

Kwak, J. Cho, S. (2005): Topological shape optimization of geometrically nonlinear structures using level set method, *Computer and Structures*, vol. 83, pp. 2257-2268.

Kang, Z., Wang, Y.Q. (2011): Structural topology optimization based on non-local Shepard interpolation of density field, *Computer Methods in Applied Mechanics and Engineering*, vol. 200; pp. 3515-3525.

Lancaster, P., Salkauskas, K. (1981): Surfaces generated by moving least squares methods, *Mathematics of Computation*, vol. 37, pp. 141-158.

Li, S., Atluri, S.N., (2008): The MLPG mixed collocation method for material orientation and topology optimization of anisotropic solids and structures, *CMES: Computer Modeling in Engineering & Sciences*, vol. 30, pp. 37-56.

Liu, G.R., Gu, Y.T. (2005): An introduction to meshfree methods and their programming, Springer, Berlin.

Luo, Z, Yang, J., Chen, L. (2006) A new procedure for aerodynamic missile designs using topological optimization approach of continuum structures, *Aerospace Science and Technology*, vol. 10, no. 5, pp. 364-373.

Luo, Z., Tong, L., Kang, Z. (2009): A level set method for structural shape and topology optimization using radial basis functions, *Computers & Structures*, vol. 228, no. 7, pp. 425-434.

Luo, Z., Zhang, N., Wang, Y. (2012): A physically meaningful level set method for topology optimization of structures, *CMES: Computer Modeling in Engineering & Sciences*, vol. 2055, no. 1, pp. 1-24.

Lin, J., Luo, Z., Tong, L. (2010): A new multi-objective programming scheme for topology optimization of compliant mechanisms, *Structural and Multidisciplinary Optimization*, vol. 40, no. 1, pp. 241-255.

Luo, Z., Zhang, N., Ji, J.C., Wu, T. (2012): A meshfree level-set method for topological shape optimization of compliant multiphysics actuators, *Computer Methods in Applied Mechanics and Engineering*, vol. 223-224, pp. 133-152.

Osher, S., Sethian, J.A. (1988): Front propagating with curvature dependent speed: Algorithms based on Hamilton-Jacobi formulations, *Journal of Computational Physics*, vol. 78, pp. 12-49.

Osher, S., Fedkiw, R.P. (2002): Level set methods and dynamic implicit surface. Springer, New York.

Pederson, C.B.W., Buhl, T., Sigmund, O. (2001): Topology synthesis of large-displacement compliant mechanisms, *International Journal for Numerical Methods in Engineering*, vol. 50, pp. 2683-2705.

Rozvany, G.I.N. (2009): A critical review of established methods of structural topology optimization, *Structural and Multidisciplinary Optimization*, vol. 37, pp. 217-237.

Sethian, J.A. (1999): Level set methods and fast marching methods: Evolving interfaces in computational geometry, fluid mechanics, computer version and material science, Cambridge University Press, Cambridge, UK.

Sethian, J.A., Wiegmann, A. (2000): Structural boundary design via level set and immersed interface methods, *Journal of Computational Physics*, vol. 163, pp. 489-528.

Sigmund, O. (1997): On the design of compliant mechanisms using topology optimization, *Mechanics of Structures and Machines*, vol. 25, pp. 493-524.

Sigmund, O. (2001): A 99 line topology optimization code written in Matlab, *Structural and Multidisciplinary Optimization*, vol. 21, pp. 120-127.

Sokolowski, J., Zolesio, J.P. (1992): Introduction to shape optimization: Shape sensitivity analysis, Springer, Berlin.

Svanberg, K. (1987): The method of moving asymptotes: a new method for structural optimization, *International Journal for Numerical Methods in Engineering*, vol. 24, pp. 359-373.

Wang, M.Y., Wang, X.M., Guo, D.M. (2003): A level set method for structural topology optimization, *Computer Methods in Applied Mechanics and Engineering*, vol. 192, pp. 227-224.

Wang, Y., Luo, Z., Zhang, N. (2012): Topological optimization of structures using a multilevel nodal density-based approximant, *CMES: Computer Modeling in Engineering & Sciences*, vol. 84, no. 3, pp. 229-252.

Yamada, T., Izui, K., Nishiwaki, S., Takezawa, A. (2010a): A topology optimization method based on the level set method incorporating a fictitious interface

energy, *Computer Methods in Applied Mechanics and Engineering*, vol. 199, pp. 2876-2891.

Zheng, J., Long, S.Y., Xiong, Y., Li, G.Y., (2008): A topology optimization design for the continuum structure based on the meshless numerical technique, *CMES: Computer Modeling in Engineering & Sciences*, vol. 29, pp. 137-154.

Zhou, M., Rozvany, G.I.N. (1991): The COC algorithm, Part II: topological, geometry and generalized shape optimization, *Computer Methods in Applied Mechanics and Engineering*, vol. 89, pp. 197-224.